Talanta 106 (2013) 408–413

Contents lists available at SciVerse ScienceDirect

Talanta

journal homepage: www.elsevier.com/locate/talanta

Electron energy loss spectroscopy investigation through a nano ablated uranium dioxide sample

Claude Degueldre [a,*], Robin Schaeublin [b], Julijana Krbanjevic [b], Eugenia Minikus [b]

[a] NES, Paul Scherrer Institut, 5232 Villigen, Switzerland
[b] CRPP, EPFL, 5232 Villigen, Switzerland

ARTICLE INFO

Article history:
Received 5 December 2012
Received in revised form
4 January 2013
Accepted 11 January 2013
Available online 14 February 2013

Keywords:
Uranium dioxide
Focused ion beam
Transmission electron microscopy
Electron energy loss spectroscopy

ABSTRACT

A lamella of uranium dioxide ($\sim 10 \times \sim 10 \times \sim 0.02$–$0.20$ μm) was produced by focused ion beam for transmission electron and electron energy loss spectroscopy (EELS) examinations. This sample allows quantitative analysis of the EEL spectra recorded for UO_2 as a function of the thickness. The M, N, O and P edges were recorded over zero loss to 4000 eV loss. The edges allow reconstruction of the electronic transitions, the lowest energy loss edges for P transitions corresponds to P3 electron transition (17.2 eV) from U6p3/2 level. The edge analysis allows also better interpretation of the loss spectrum with identification of the plasmon peak of the core electron transition edges. In addition, the energy lost was studied through a range of thicknesses going from ~20 to ~200 nm to derive the electron mean free path and cross section for inelastic scattering in the plasmon part of the spectrum. The mean free path of inelastic electron for uranium dioxide is compared with that reported earlier for other oxides from Be to Bi and for 200 keV incidents electrons. The present study emphasises the potential of combining FIB and EELS for the analysis of actinide compounds.

1. Introduction

Transmission electron microscopy (TEM) has been used for decades to characterize actinide materials [1], in particular uranium dioxide. Uranium exhibits several valence states and the reduction of U(VI) and U(V) species by electrons in nanometer powders of uranium oxide was addressed in the studies of UO_2 oxidation [2]. This original method makes it possible to synthesize by reduction under anoxic conditions nanometer UO_2 powders with a calibrated size. The powder characterization by X-ray diffraction, X-ray photoelectron spectroscopy and TEM shows the formation of spherical crystallites of UO_{2+x} of about 5 nm in size.

Single crystals of uranium dioxide, deformed under compression up to embrittlement, were examined by TEM [3]. They revealed dislocation structures consisting of numerous dipoles and dipolar loops. Particular features were noted in the dislocation arrangements which can be related to several of the theories of dipole formation. It has also been analysed using electron energy loss spectroscopy (EELS) [4]. In another study, corroded spent uranium oxide fuel showed in TEM and EELS enriched region contained U, Am, Ru, Zr and minor amounts of rare earth elements [5]. Precipitated uranium oxide phases identified as U_3O_8 were characterized by EELS using M (e.g., 3d→5f) and N (e.g., 4d→5f) edges recorded for the nano-crystals, between U(VI) secondary phases and the corrosion surface. These authors use the M_5/M_4 ratio to estimate the redox of U in the oxides.

Another work reports an EELS analysis from phase-specific regions of U metal and UO_2 [6]. The $N_{4,5}$ (i.e., 4d→5f) spectra were analyzed using the spin–orbit sum rule. The results show that the technique is sensitive enough to detect changes in the branching ratio of the white-line peaks between the metal and dioxide of uranium. The data suggest that the metal–oxide bonds in UO_2 are strongly covalent in nature and do not exhibit an integer valence change as would be expected from purely ionic bonding.

Core-loss EELS results suggest that tetravalent uranium compounds have an energy loss resolvable from hexavalent compounds. Indeed, as shown in e.g., [7], shoulders of the uranium $O_{4,5}$ edge (e.g., 5d→5f) allows distinguishing UO_2 from UF_4. In the presence of carbon, correction techniques must be applied. However, low-loss spectrum characteristics allow distinguishing the carbon from a holey substrate from the uranium oxide specimens. Uranium oxides, fluorides, and minerals show a tendency of reduction of uranium toward 4+ under the electron beam. The conditions for low-loss analysis need to be as vigorous as those for core losses. They need to be done without altering the valence of most oxides. From a systematic investigation point of view it must be noted that the uranium P_{1-3} transitions were however never reported by EELS.

The connection between the experimentally observed electron energy loss spectra and elevated temperature scanning tunneling images of surfaces of semiconducting uranium dioxide UO_2 was

* Corresponding author. Tel.: +41 56 310 41 76.
E-mail address: claude.degueldre@psi.ch (C. Degueldre).

0039-9140/$ - see front matter © 2013 Elsevier B.V. All rights reserved.
http://dx.doi.org/10.1016/j.talanta.2013.01.023

also analysed [8]. The combination of electron energy loss spectroscopy, atomic-resolution tunneling imaging and first-principles *ab initio* calculations was shown to provide a powerful tool for studying electronic and structural properties of surfaces of actinide oxides. EELS can consequently provide information on the structure of UO_2 that can be precious for the analyses of the thermal conductivity in terms of lattice, radiation and electronic components such as recommended [9].

The actinide compound samples for EELS investigation in the TEM (mainly at low energy) require careful preparation such as that provided by focused ion beam (FIB). This technique is based on deposition and ablation of materials. FIB systems operate in a similar fashion to a scanning electron microscope (SEM) except that it uses a finely focused beam of ions (usually gallium). It can be operated at low beam currents for imaging or high beam currents for site specific sputtering or milling. Since about 10 years FIB is widely used routinely for the preparation of electron transparent thin specimens, adequate for TEM investigations.

However, it should be noted that FIB development started more than 40 years ago and was applied for sputtering and thin film deposition in few laboratories. In the late 1970s two FIB sputtering units were used in CEA for preparing actinide targets [10]. Both were mounted in glove boxes. One apparatus was used for low specific activities, i.e., Th and U isotopes and the other for high specific activities, i.e., Pu and trans-Pu isotopes. Both were used for metals, oxides or other chemical forms of actinide deposits as thin films. Further sputtering work was carried out at CEA in the 1980s [11]. Targets were prepared for very precise specifications. These thin film deposits were made of actinides from Th to Cf. In the US, thin film production of 'alpha emitters' samples were also performed in the 1980s. Again ion beam sputtering was utilised for the preparation of thin films used as targets. Work was carried out in the Isotope Research Materials Laboratory at ORNL [12] to prepare actinide targets up to 100 $\mu g\ cm^{-2}$ by ion beam sputtering and thin film deposition.

More recently at AWE [13], FIB was required for site specific TEM sample extraction to examine using electron spectroscopy the composition and surface structure of uranium welded by an electron beam. Surface composition to a depth of a few microns was determined using SIMS profiling, and direct thickness measurements of surface over-layers on the metal were made using FIB. Here the material was cleaned up by FIB abrasion; no micro-samples were however produced by FIB.

In the present work, uranium dioxide was investigated by EELS in order to determine the valence state of uranium for a better understanding of its electronic structure in the redox state. Specimens were extracted by FIB. The EELS data produced in this study would never be gained without the high quality of the samples produced by FIB. Requirement of FIB samples are a well defined geometry and quality, i.e., contamination free.

2. Experimental and data treatment

The investigated sample was a UO_2 polycrystalline piece. The sample preparation by FIB, the TEM observations and EELS measurements were done at the electron microscopy laboratory (EML) at PSI. The EML was recently upgraded under the initiative of the author for handling of alpha isotope material with an activity below 100 LA (limit of autorisation) corresponding to a C-Lab, allowing the work on small actinide sources.

2.1. Focused ion beam

The FIB work was carried out with a Zeiss Nvision 40 Cross-beam workstation. It includes both a focused ion beam and a scanning electron microscope. The FIB unit operates with a source of Ga^+ ions that can be accelerated from 1 to 30 kV; the SEM unit operates from 0.5 to 30 kV. The FIB resolution reaches 4 nm for 30 kV and 1.6 nm for the SEM at 30 kV. The minimum usable Ga^+ ion beam size is 4 nm. The unit is completed with an Oxford Instruments energy-dispersive spectrometer (X-ray EDS) unit for elemental analysis. The instrument includes: a chamber SE detector, an Inlens EsB detector, an Inlens SE detector, a STEM detector, a 4Q BSD detector, and a cryo stage from Gatan.

2.2. Transmission electron microscopy and electron energy loss spectroscopy

The transmission electron microscope is a JEOL 2010 type TEM unit equipped with a LaB_6 electron gun and operated at 200 keV. The TEM point to point resolution is 2.3 Å. The TEM unit is equipped with a Gatan Enfina electron energy loss spectrometer. The EELS energy resolution was 0.5–1.0 eV in the studied domain. EEL spectra images were taken by Gatan Orius 11Mpixels CCD camera.

The EELS data were acquired and worked out using Gatan's EELS analysis tools included in Gatan DigitalMicrograph software. The analysis routines follow, wherever possible, a similar (or often identical) approach to that adopted in EL/P. Continuing the underlying philosophy of EL/P, the EELS analysis routines encapsulate many details in a few high-level commands. For instance, once a spectrum from 0 to about 500 eV, including the zero loss peak (ZLP) has been acquired, the menu 'thickness measurement' in DigitalMicrograph® may be used to evaluate the local sample thickness with a precision of 10%.

3. Results

3.1. Sample preparation by focused ion beam

The piece of uranium dioxide is a sample of non-irradiated fuel (UO_2) material. The sample has a tier like shape with sizes around 1.9 mm, 2.3 mm and 2.2 mm for the arc of 57°. The thickness of the tier was 0.25 mm. Its total activity does not exceed 0.9 LE (limit of exemption). The sample was glued with C glue on a typical SEM Al stub. The sample was first examined using the SEM instrument of the NVision 40. The trapezoidal machining of the sample necessary for the extraction of the thin lamella was carried out using 30 kV accelerated Ga^+ ions. For a current of 30 nA, 10 μm were eroded in 14 min, corresponding to an ablation rate of $\sim 10\ nm\ s^{-1}$, which is fast compared to light element material erosion (e.g., SiO_2 or $Si_4Al_2O_{11}$). The coarse lamella, about 1 μm thick, now liberated on 3 sides was subsequently freed from below using lateral–diagonal ion milling.

Once the coarse sample was prepared, the transfer needle was approached and attached using carbon strip produced by deposition of carbon from a precursor gas decomposed by the ion beam. This allowed fixing the sample in order to proceed to its complete liberation by ablation of the 4th side. The coarse lamella was subsequently lifted and approached to the TEM sample carrier made of a 3 mm half moon holding a comb like structure, the so-called 'omniprobe grid'. The specimen is fixed by carbon coating to one of the comb teeth. It was then freed from the transfer needle by sputtering away the carbon strip on the needle side.

The attached TEM lamella was then shaped to an edged lamella with variable thickness, allowing for the study of the thickness dependence of the EELS signal. For the fine milling to the final polishing, the ablation was carried out with a 2 kV Ga^+ ion current of 80 pA and with an incident angle from 30° to 1°. The TEM lamella sample was a $10 \times 10 \times (0.030–0.300)$ μm surrounded by

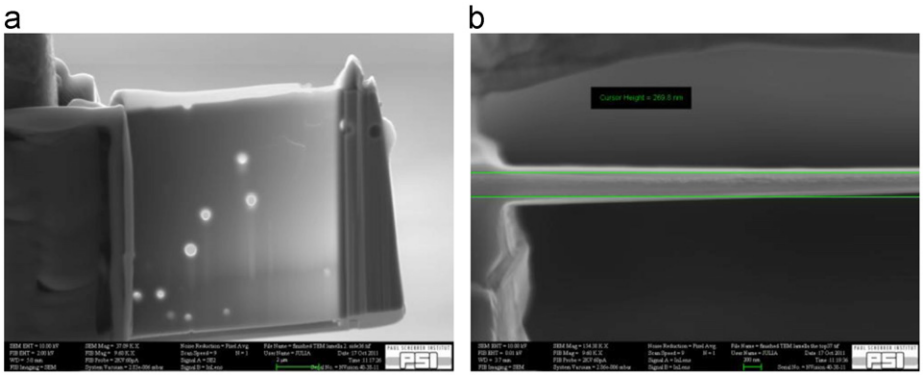

Fig. 1. SEM view of the TEM lamella attached to the TEM omniprobe grid: (a) top view (b) side view. Fine milling and polishing at 2 keV and 80 pA Ga^+ ion beam.

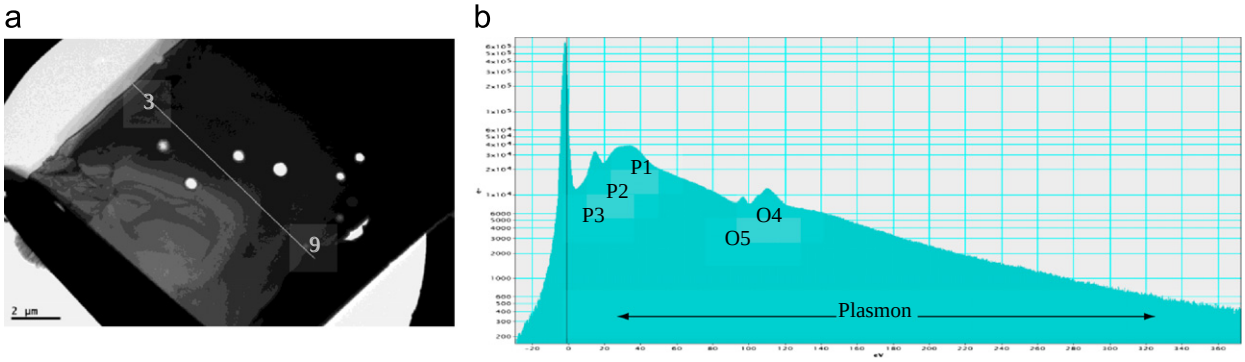

Fig. 2. (a) TEM micrograph of the UO_2 lamella labeled (line) with thicknesses and (b) corresponding EELS spectrum. Conditions: incident electron 200 kV. Thicknesses in zone 3: 55 nm in zone 9: 265 nm.

thicker edges for mechanical support (see Fig. 1). It should be noted that during preparation the abrasion is made using diagonal incidence that reduces the impact of gallium from the point of view of damage and contamination. Both implantation and damage data described in the following are estimated for an orthogonal implantation, which correspond to a maximum in our conditions.

3.2. Electron- microscopy and energy loss spectroscopy

The FIB produced sample was examined by TEM prior to EELS analysis. The locations of the various domains with respective thicknesses ranging from ~60 to ~260 nm are located on line drawn on the lamella (see Fig. 2a).

The EELS spectrum shown in Fig. 2b is plotted on a log scale. It reveals the following features:

- the zero loss energy peak
- the plasmon part of the spectrum and
- the core loss electron edges

Interestingly, the EELS spectrum shows in the shoulder of the plasmon the P_3 edge of U that peaks at 17.2 eV. The plasmon hump partially masks the two other possible P edges, namely P_2 and P_1 edges at 29.0 and 35.3 eV, respectively, as well as the known L edge of O at 42 eV. This statement on the P_3 edge is carefully assessed in the discussion section, as these U P peaks were never reported in the EELS literature.

The $O_{4,5}$ edges of U however are known and are to be found at 98.7 and 112.5 eV, respectively, similar to the data reported by Moore and van der Laan [7]. The other U edges recorded at higher energy are identified to be the N and M edges as already reported in the literature [5].

The results gained for the core edges and in the plasmon peak are discussed in Section 4.2.

4. Discussion

4.1. Ion—Uranium dioxide interactions

In order to evaluate the contamination and damage of the UO_2 TEM lamella by the FIB, the stopping power of UO_2 was investigated using SRIM2011 for two of the Ga^+ ion energies applied during ablation. SRIM modeling allows estimation of the penetration profile and damage after 5×10^6 ions (see results Fig. 3).

- For the 2 keV Ga^+ ions the penetration depth ranges from 2 to 4 nm and a damage of 0.4 collision per Ga^+ ion and per Å is found in this domain. This result justifies the use of 2 kV Ga^+ ions for the production of 100 nm size samples since the affected domain (damage and Ga contamination) reaches only 2 nm in depth.
- For the 30 keV Ga^+ ions the penetration depth is 10 to 20 nm and a damage of about 1.2 collision per ion (Ga^+) and per Å is found for these depths. This result justifies the use of 30 kV Ga^+ ions for the production of μm size samples because the affected zone (damage and Ga contamination) reaches only 20 nm depth.

Note for comparison that for the 30 keV Ga^+ ions in SiO_2 the penetration is about 25 nm.

4.1.1. Energy transfer

The interaction of Ga^+ in the UO_2 induced an adiabatic energy conversion (5×10^{-15} J per 30 keV Ga^+) within the penetrated volume of fuel. Prior to relaxation, this induces thermal spike with

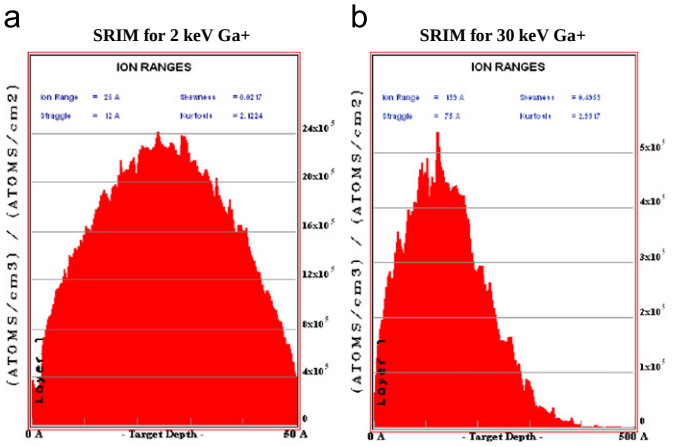

Fig. 3. Penetration depths of (a) 2 kV and (b) of 30 kV accelerated Ga^+ in UO_2.

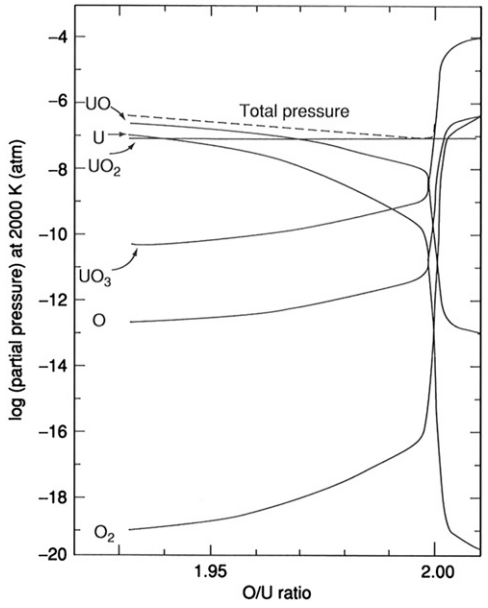

Fig. 4. Partial pressures and total pressure over $UO_{2(\pm 1)}$ of various compositions at 2000 K (from Storms [16]).

temperature of the order of thousands of K for some ps. For understanding the behaviour of fuel material under Ga^+ ion irradiation during sample preparation, it is important to take into account the thermo-physical (thermal conductivity, heat capacity) response of the material. The thermal conductivity of UO_2 (irradiated or not) is well known. An average value of $2\,W\,m^{-1}\,K^{-1}$ (according to Ref. [14]) may be used for energy transfer calculation. For SiO_2 the thermal conductivity is $\sim 1.5\,W\,m^{-1}\,K^{-1}$ [15] consequently its sputtering rate should be comparable.

4.1.2. Chemical interactions

The interaction of Ga^+ in UO_2 induced chemical reactions at temperatures of the order of 1000 to 2000 K. Since Ga^+ is a reducing agent one could expect that reactions such as:

$$2Ga^+ + 3UO_2(s) \Leftrightarrow Ga_2O_3(g) + 3UO(g)$$

and

$$2Ga^+ + UO_2(s) \Leftrightarrow Ga_2O(g) + 3UO^{2+}$$

take place.

The uranium chemical activity has been measured between 1667 and 2175 K see Ref. [16], and between $U(l) + UO_{2-x}$ and $UO_{2.0}$ using a mass spectrometer to study the behavior of UO(g) (see Fig. 4). Clearly the formation of UO may favorize the abrasion in the fuel. Such reactions are less favorable with SiO_2 and Al_2O_3. SiO forms only at temperature around 3000 K [17]. This difference in chemical behaviour could explain the fast abrasion of fuel material.

4.2. Electron—Uranium dioxide interactions

4.2.1. Electronic configurations and transitions

The external electronic configuration of U^{4+} is $5f^2$ [18]. The full electron configuration of U^{4+} in UO_2:

$1s^2$, $2s^2p^6$, $3s^2p^6d^{10}$, $4s^2p^6d^{10}f^{14}$, $\mathbf{5s^2p^6d^{10}f^2}$, $\mathbf{6s^2p^6d^0}$, $\mathbf{7s^0}$ corresponding to the K L M N O P transitions, respectively.

However the ion electronic configuration has to be completed for the molecular orbitals.

The study of small actinide molecules presents a challenge for experimental and theoretical chemists. The nearly degenerated 5f, 6d, 7s, and 7p orbitals give rise to a multitude of possible configuration interactions and a dense manifold of low-lying states, which complicates computations and renders assignment of experimental spectra difficult. A joint effort of experimentalists and theoreticians is therefore needed to resolve the electronic structure of these systems. The situation is more complicated for the UO_2 molecule. Likely candidates for the ground state are the $5f^17s^1$ 3u and the $5f^2$ 3Hg states. Both orbitals are non-bonding but the 7s orbital is more diffuse, leading to stronger and shorter bonds [19,20].

The EEL spectrum (see Fig. 2) was quantitatively studied for its peak intensity (Fig. 5) and energy as a function of the thickness. All peak intensity increases rapidly with the thickness up to a maximum followed by a decrease as expected (see Fig. 5). The peak energy at 17.2 ± 0.3 eV ascribed to the P_3 edge of U was observed to be invariant of the thickness. This supports the concept of P core electron transition since a plasmon peak is thickness dependant e.g., [21]. Any energy changes due to degeneration, hybrid or molecular orbital formation are rather small. In addition the electronic

population is fed by the primary electron flux. The plasmon hump partially masks the 2 other P edges, namely P_2 and P_1 edges at 29.0 and 35.3 ± 0.6 eV, respectively (P_2 is however ill defined), as well as the known L edge of O at 42 eV.

The electron binding energy values are U5f (2 eV), O2p (6 eV), U6p3/2 (18 eV), O2s (24 eV) and U6p1/2 (30 eV) according to Veal and Lam Ref. [22,23].

In the Handbook of Chemistry and Physics [24] the listed energies for the P_1, P_2, and P_3 edges were 70.7, 42.3, and 32.3 eV, respectively. They were corrected in the last version of the CRC Handbook [24] with values of 43.9, 26.8 and 16.8 eV as reported in Ref. [25]. In this study, the reported values are listed at 17.2, 27.0, and 35.3 eV which are reasonable.

The O_5 and O_4 edges were found at 98.7 ± 0.9 and 112.5 ± 0.6 eV, respectively, and comparable (97.5 and 111.3 eV) with the data provided in Ref. [7] while electron binding energy values are 94.2 and 102.8 eV from Ref. [25]. Again, the peak maximum intensities were found to increase (from zero thickness) toward a maximum (depending on the peak energy) and to decrease when thickness increases (see Fig. 5).

The interactions of low-energy X-rays within condensed matter, viz. photoabsorption and coherent scattering, have been described for photon energies outside the absorption threshold regions by using atomic scattering factors. Table 1 presents the edges observed by EELS and/or XAFS for the element electronic transitions of UO_2.

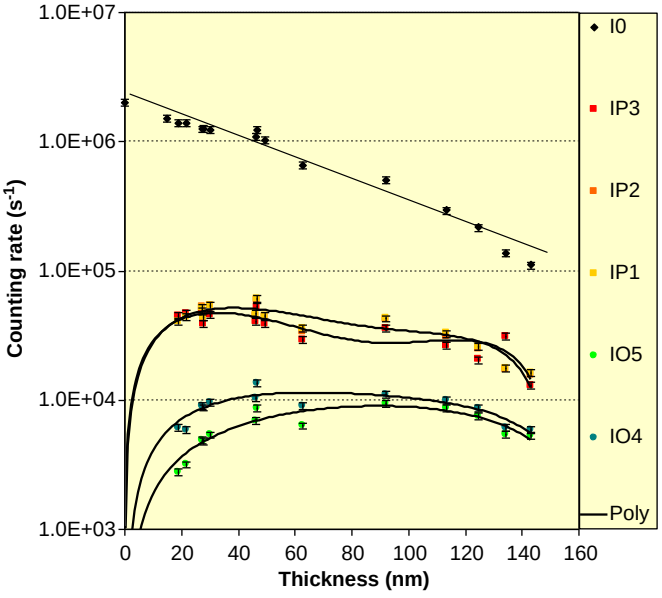

Fig. 5. EELS peak intensities recorded for various UO_2 thicknesses. Conditions: energy of incident electron 200 keV, electron energy calibration at zero loss, β: 5 mrad, θ: 5 mrad, aperture 3 mm, current density 30 pA cm^{-2}, electron spot on object ~15 nm.

4.2.2. Electron free path.

The electron free path for inelastic scattering, λ, from a scattered electron beam through thickness t may be evaluated using [30]:

$$t/\pi = \ln(I_{tot}/I_z) \quad (1)$$

with I_z: the peak intensity at zero loss and I_{tot}: the total intensity through the all spectrum.

The atomic scattering factors may be accurately determined from the atomic photoabsorption cross sections using modified Kramers–Kronig dispersion relations. t (nm) becomes:

$$t = \frac{4a_0FE_0}{I_0(1-1/n^2)}\int \frac{S(E)dE}{E\ln(1+\beta^2/\theta^2)} \quad (2)$$

with a_0 the Bohr radius (nm), F a relativistic factor, E_0 the beam energy, I_0 the zero-loss intensity, n the breaking index for visible light (−), $S(E)$ the single scattering distribution, β collection semi-angle (rad) and θ characteristic scattering angle at an energy E.

The EELS data analysis is even easier with the log-ratio method, however, absolute calibration of this method requires knowledge of λ. It can be expressed in terms of the inelastic scattering cross section per molecule, σ_i, on the basis of atom/molecule density $\mathcal{N}$:

$$\lambda = (\mathcal{N}\,\sigma_i)^{-1} \quad (3)$$

The latter has been measured here in a wide range of solids e.g., [31].

For the investigated sample of UO_2, the average atomic number Z is 36. For the accelerating voltage E_0 200 kV and a collection semi-angle β of 10 mrad, F of 0.61762 and an E_{av} of 27.61 eV, a value for λ of 95.30 nm may be estimated.

The thicknesses measured in SEM (Fig. 1) and deduced from EELS spectrum of selected zones may be compared in Table 2.

Mean free path of inelastic electron scattering λ has been measured with a 200 keV transmission electron microscope for the majority of stable elemental solids and their oxides [32]. An oscillating behavior vs. atomic number Z has been observed, such that within one row of the periodic table, the minimum

Table 2
Comparing SEM and EELS thickness.

Zone (see Fig. 2)	9	3
SEM thickness (nm)	265 ± 5	55 ± 5
EELS thickness (nm)	263 ± 15	67 ± 6

Table 1
UO_2 absorption edges. data from X-ray interactions for Z=1–92, from Ref. [26].

Element	**U**	**U**	**O**	**U**	**U**	**U**	**O**	**U**	**U**	**U**	**U**
Transition	**P**	**P**	**L**	**O**	**O**	**O**	**K**	**N**	**M**	**L**	**K**
Energy (eV)	**17.2**	16.8	41.6	**98.7**	97.5	94.2	543.1	377.4	3552	17,166	115,606
	29.0	26.8		**112.5**	111.3	102.8		388.2	3728	20,948	
	35.3	43.9				192		736.2	4303	21,757	
						257		778.3	5182		
						321		1043	5548		
								1271			
								1439			
Method	EELS	(XPS)	EELS	EELS	EELS	EELS (XAFS)	EELS XAFS	EELS XAFS	(EELS) XAFS	XAFS	XAFS
References	*	[25]	[25]	*	[7]	[25]	[25]	[25]	[25]	[27,28]	[29]

* This work.

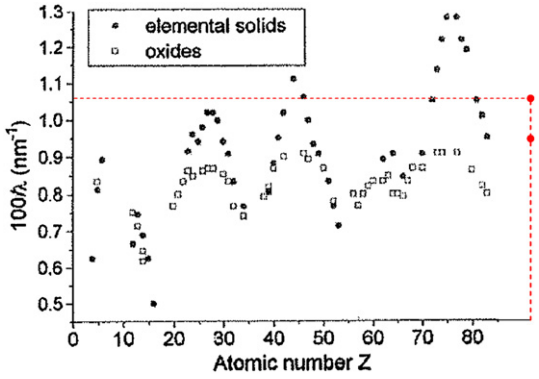

Fig. 6. Mean free path of inelastic electron scattering in elemental solids and oxides. Black dots: from Ref. [32], red dots: our data for uranium dioxide. High value: raw data, low value: with 10% core shell correction. (For interpretation of the references to color in this figure legend, the reader is referred to the web version of this article.)

(maximum) of λ is observed for elements with completed (empty) outer d shells. A significantly weaker $\lambda(Z)$ dependence is observed for the oxides. The $\lambda(Z)$ variation is ascribed to the three major factors, namely the atomic density, the number of "free" electrons per atom, and the contribution of atomic core-loss transitions.

From a synthesis of the currently available experimental data and recent theoretical calculations for photo-absorption, the angle-independent, forward-scattering components of the atomic scattering factors have been thus semi-empirically determined and tabulated here for 92 elements and for the region 50–30,000 eV. Atomic scattering factors for all angles of coherent scattering and at the higher photon energies are obtained from these tabulated forward-scattering values by adding a simple angle-dependent form-factor correction. The incoherent scattering contributions that become significant for the light elements at the higher photon energies are similarly determined. The basic X-ray interaction relations that are used in applied X-ray physics are presented here in terms of the atomic scattering factors (see Ref [26]). On this basis, the mean free path of inelastic electron scattering in UO_2 is compared in Fig. 6 with that found in elemental solids and oxides by Iakoubovskii et al. [32].

Finally, in pure UO_2 solid multiple scattering may be expected as observed by Buck et al. [33]. This effect that would result in the occurrence of the U-P edge added to other edges, such as the M-edge, or the oxygen K-edge was not evidenced by secondary peaks in the thicker regions.

5. Conclusion

The production of a clean TEM lamella of uranium dioxide with sizes of $\sim$10 μm × 10 μm × $\sim$0.02–0.20 μm was successfully achieved by focused ion beam. Quantitative investigations by electron- microscopy and energy loss spectroscopy have been performed. These samples allow detailed investigations of the EEL spectra recorded not only for the UO_2 itself but also as a function of the lamella thickness. The M, N, O and P edges were recorded over the 0–4000 eV energy range. The edges allow reconstruction of the electronic transitions, the later P_3 and P_2 at 17.2 ± 0.3 eV and at 29.0 ± 0.6 eV corresponding to the electron transitions from the U6p3/2 and U6p1/2 levels. The edge analysis allows a better modeling and understanding of the EELS spectrum as well as a better separation of the plasmon part from the core electron transition edge. In addition, the energy lost was studied through the range of thicknesses going from 20 to 200 nm to derive the electron mean free path and cross section for inelastic scattering in the plasmon part of the spectrum. The inverse of mean free path of inelastic electron for uranium dioxide is compared with that of reported earlier for other element oxides and for electron incident energy of 200 keV.

In future work the authors shall investigate the other actinide dioxide as well as the oxides from other valence state of uranium. These studies generate key results that can be used for the analysis of nuclear fuels at the nanometer scale.

Acknowledgements

The authors thank the radioprotection officers, especially Mr Tobias Schneider for upgrading the Electron Microscopy Lab at PSI for alpha emitter handling. Mr Matthias Martin is thanked for providing of the UO_2 sample.

References

[1] K.T. Moore, Micron 41 (2010) 336–358.
[2] G. Rousseau, M. Fattahi, B. Grambow, L. Desgranges, F. Boucher, G. Ouvrard, N. Millot, J.C. Nièpce, J. Solid State Chem. 182 (2009) 2591–2597.
[3] C.S. Yust, C.J. McHargue, J. Nucl. Mater. 31 (1969) 121–137.
[4] St B. Rice, H.H. Bales, J.R. Roth, A.L. Whiteside, Microsc. Microanal. 5 (1999) 437–444.
[5] E.C. Buck, P.A. Finn, J.K. Bates, Micron 35 (2004) 235–243.
[6] K. Moore, G. van der Laan, R. Haire, M. Wall, A. Schwartz, Phys. Rev. B: Condens. Matter 73 (2006) 033109–033112.
[7] K.T. Moore, G. van der Laan, Ultramicroscopy 107 (2007) 1201–1206.
[8] S.L. Dudarev, M.R. Castell, G.A. Botton, S.Y. Savrasov, C. Muggelberg, G.A.D. Briggs, A.P. Sutton, D.T. Goddard, Micron 31 (2000) 363–372.
[9] G.J. Hyland, J. Nucl. Mater. 113 (1983) 125–132.
[10] J. Kwinta, Nucl. Instrum. Methods 167 (1979) 65–70.
[11] J. Kwinta, P.H. Brossard, J.J. Michel, J. Thoreux, Inorg. Chim. Acta 94 (1984) 119–120.
[12] W.S. Aaron, L.A. Zevenbergen, H.L. Adair, Nucl. Instrum. Methods Phys. Res., Sect. A 236 (1985) 520–525.
[13] J.R. Petherbridge, T.B. Scott, J. Glascott, C. Younes, G.C. Allen, I. Findlay, J. Alloys Compd. 476 (2009) 543–549.
[14] M. Amaya, M. Hirai, J. Nucl. Mater. 247 (1997) 76–81.
[15] I.M. Abdulagatov, S.N. Emirov, T.A. Tsomaeva, A. Gairbekov, S.Ya. Askerov, N.A. Magomedova, J. Phys. Chem. Solids 61 (2000) 779–787.
[16] E.K. Storms, J. Nucl. Mater. 13 (1985) 231–243.
[17] T. Watanabe, M. Soyama, A. Kanzawa, A. Tukenchi, M. Koike, Thin Solid Films 345 (1999) 161–166.
[18] D. Ippolito, L. Martinelli, G. Bevilacqua, Phys. Rev. B: Condens. Matter 71 (2005) 064419–064422.
[19] I. Infante, E. Eliav, M.J. Vilkas, Y. Ishikawa, U. Kaldor, L. Visscher, J. Chem. Phys. 127 (2007) 124308–124311.
[20] F. Zhou, V. Ozolins, Phys. Rev. B: Condens. Matter 83 (2011) 085106–085109.
[21] J.A. Scholl, A.L. Koch, J.A. Dionne, Nature 483 (2012) 421–427.
[22] B.W. Veal, D.J. Lam, Phys. Rev. B: Condens. Matter 10 (1974) 4902–4908.
[23] B.W. Veal, D.J. Lam, Phys. Lett. 49A (1974) 466–468.
[24] CRC Handbook of Chemistry and Physics (63rd ed.).
[25] X-RAY DATA BOOKLET, Center for X-ray Optics and Advanced Light Source, Lawrence Berkeley National Laboratory (2009).
[26] B.L. Henke, E.M. Gullikson, J.C. Davis, At. Data Nucl. Data Tables 54 (1993) 181–342.
[27] C. Degueldre, G. Kuri, M. Martin, A. Froideval, S. Cammelli, A. Orlov, J. Bertsch, M.A. Pouchon, Nucl. Instrum. Methods Phys. Res., Sect. B 268 (2010) 3364–3370.
[28] 〈http://cars9.uchicago.edu/~ravel/software/doc/Standards/u6.html〉.
[29] T.h. Materna, J. Jolie, W. Mondelaers, B. Masschaele, Radiat. Phys. Chem. 59 (2000) 449–457.
[30] R.F. Egerton, Electron Energy-Loss Spectroscopy in the Electron Microscope, second ed., Springer, 1996 305.
[31] K. Iakoubovskii, K. Mitsuishi, Y. Nakayama, K. Furuya, Microsc. Res. Tech. 71 (2008) 626–631.
[32] K. Iakoubovskii, K. Mitsuishi, Y. Nakayama, K. Furuya, Phys. Rev. B: Condens. Matter 77 (2008) 104102–104109.
[33] E.C. Buck, M. Douglas, R.S. Wittman, Micron 41 (2010) 65–70.